Scattering resonances in slow NH3–He collisions

Koos B. Gubbels, Sebastiaan Y. T. van de Meerakker, Gerrit C. Groenenboom, Gerard Meijer, and Ad van der Avoird

Citation: The Journal of Chemical Physics **136**, 074301 (2012); doi: 10.1063/1.3683219
View online: http://dx.doi.org/10.1063/1.3683219
View Table of Contents: http://scitation.aip.org/content/aip/journal/jcp/136/7?ver=pdfcov
Published by the AIP Publishing

Scattering resonances in slow NH_3–He collisions

Koos B. Gubbels,[1,2,a)] Sebastiaan Y. T. van de Meerakker,[2,1] Gerrit C. Groenenboom,[2] Gerard Meijer,[1] and Ad van der Avoird[2,b)]
[1]*Fritz-Haber-Institut der Max-Planck-Gesellschaft, Faradayweg 4-6, D-14195 Berlin, Germany*
[2]*Radboud University Nijmegen, Institute for Molecules and Materials, Heyendaalseweg 135, 6525 AJ Nijmegen, The Netherlands*

(Received 15 November 2011; accepted 19 January 2012; published online 15 February 2012)

We theoretically study slow collisions of NH_3 molecules with He atoms, where we focus in particular on the observation of scattering resonances. We calculate state-to-state integral and differential cross sections for collision energies ranging from 10^{-4} cm^{-1} to 130 cm^{-1}, using fully converged quantum close-coupling calculations. To describe the interaction between the NH_3 molecules and the He atoms, we present a four-dimensional potential energy surface, based on an accurate fit of 4180 *ab initio* points. Prior to collision, we consider the ammonia molecules to be in their antisymmetric umbrella state with angular momentum $j = 1$ and projection $k = 1$, which is a suitable state for Stark deceleration. We find pronounced shape and Feshbach resonances, especially for inelastic collisions into the symmetric umbrella state with $j = k = 1$. We analyze the observed resonant structures in detail by looking at scattering wavefunctions, phase shifts, and lifetimes. Finally, we discuss the prospects for observing the predicted scattering resonances in future crossed molecular beam experiments with a Stark-decelerated NH_3 beam. © *2012 American Institute of Physics*. [http://dx.doi.org/10.1063/1.3683219]

I. INTRODUCTION

The tremendous experimental progress in performing scattering experiments has evolved to the point where it is nowadays possible to study collisions between particles in the laboratory over an energy range of about 25 orders of magnitude. The collisions of highest energy are produced by modern charged-particle accelerators reaching the TeV range, while the collisions of lowest energy are studied in ultracold atomic quantum gases going all the way down to the nK regime. In both types of collision experiments, scattering resonances play an important role. In high-energy collisions, a resonance in the cross section caused by the formation of an intermediate bound state is a direct way to detect previously unseen particles. In ultracold atomic scattering, the energy of an intermediate bound molecular state to be formed during the collision can sometimes be accurately tuned by applying an external magnetic field. As a result, the scattering length of low-energy *s*-wave collisions gets under full experimental control, giving rise to a unique quantum many-body environment with a completely tunable interaction parameter.[1,2]

Because molecules are typically harder to manipulate than atoms and charged particles, the observations of resonances in molecular beam scattering have been limited to a few rare cases.[3–8] However, in recent years rapid progress has been made in performing high-precision cold molecular scattering experiments due to the application of the Stark deceleration technique to the study of molecular collisions.[9] A Stark decelerator operates according to the same principles as a linear charged-particle accelerator, where the dipolar or Stark force is used to decelerate neutral polar molecules with time-varying electric fields.[10] With the Stark decelerator it is possible to generate almost perfectly quantum-state selected molecular beams with a computer-controlled final velocity and a small longitudinal velocity spread. By applying this technique to the scattering of the OH radical with rare gas atoms, such as Xe,[9] Ar,[11] and He,[12] the threshold behavior for inelastic scattering into the first excited rotational levels of OH could be accurately determined. Excellent agreement was found with cross sections obtained from close-coupling calculations using *ab initio* potential energy surfaces (PESs).[9,11,13] In the same way, also cold inelastic collisions of OH radicals with D_2 molecules were studied experimentally.[12]

In this article, we study in detail cold collisions between NH_3 molecules and He atoms. The ammonia-He system is a van der Waals complex, and in general the (quasi-)bound states of such complexes are sensitive to the interaction potential. As a result, high-resolution spectroscopy on van der Waals complexes has been an important tool for increasing our understanding of intermolecular forces.[14,15] High-precision scattering experiments are a very promising additional tool for obtaining detailed information on potential energy surfaces. At higher scattering energies the short-range repulsive part of the interaction is mainly probed, while at very low collision energies the long-range part of the potential is dominant in determining the scattering behavior. Moreover, scattering resonances give important information on the energy of quasi-bound states that are sensitive to potential wells at mid-range interparticle distances. This shows that large parts of the potential energy surfaces can be accurately probed by cold collision experiments. Recent scattering

a)Electronic mail: K.Gubbels@science.ru.nl.
b)Electronic mail: A.vanderAvoird@theochem.ru.nl.

experiments have indeed been able to distinguish between PESs that were only of good quality and PESs that were of excellent quality.[11,13] A very different experiment in which the NH_3-He interaction plays an important role, is the trapping of NH_3 molecules inside He nanodroplets to perform high-resolution spectroscopy.[16]

Rotational energy transfer by cold collisions is an important process in various astrochemical environments, such as interstellar clouds and cold exoplanetary atmospheres. Since the first identification of NH_3 molecules in the interstellar medium,[17] ammonia has been detected in several gas-phase astrochemical spectra. The rate coefficients of NH_3-He scattering are an important ingredient for a numerical modelling of astrochemical environments. This is one of the reasons why NH_3-He collisions have been studied experimentally[18–22] and theoretically[23–28] by several groups. The most recent scattering calculations have been performed with the potential energy surface of Hodges and Wheatley.[29] However, in order to get agreement with experimentally determined virial coefficients, this potential had to be scaled by a rather large factor.[26] The same potential has also been used to theoretically study low-energy NH_3-He collisions, where strong scattering resonances were observed for various initial and final states of the NH_3 molecule.[28] Unfortunately, the initial state that is most suitable for Stark deceleration was not considered. This is namely the state $|jk\pm\rangle = |11-\rangle$, where j is the angular momentum of the ammonia molecule, k is the projection on its threefold symmetry axis, and $\pm$ refers to its symmetric/antisymmetric umbrella inversion tunneling state. For the energy level diagram of the ammonia molecule, see Fig. 1. Moreover, in the study of Ref. 28 ammonia was treated as a rigid molecule, implying that the umbrella inversion motion of the NH_3 molecule was not considered.

In this article, we study all possible elastic and inelastic scattering processes at low collision energies using $|11-\rangle$ as an initial state of the *para* NH_3 molecule. For *para* ammonia, k is either 1 or 2 (modulo 3), while for *ortho* ammonia, k is equal to 0 (modulo 3). We note that the nuclear spin configurations for the *para* ammonia molecules have a smaller statistical weight than those for the *ortho* ammonia molecules. For the considered initial state, we find that particularly the inversion inelastic scattering to the $|11+\rangle$ state gives rise to pronounced resonant structures that are promising to be observed experimentally in crossed beam experiments. We start by introducing the theoretical framework for studying the atom-molecule collisions. After this, we present a new NH_3-He potential using the most recent developments in electronic structure calculations. We describe the numerical methods to fit the potential, after which we present the calculations of the integral and differential cross sections. In both cross sections, we find rapid variations as a function of energy, which are clear signs of resonant behavior. To determine the origin of these resonances, we perform bound state calculations as well as reconstructions of the full scattering wavefunctions. The phase shifts and the lifetimes are also determined near resonance. Finally, we comment on the prospects of observing these scattering resonances in the NH_3-He system in the near future.

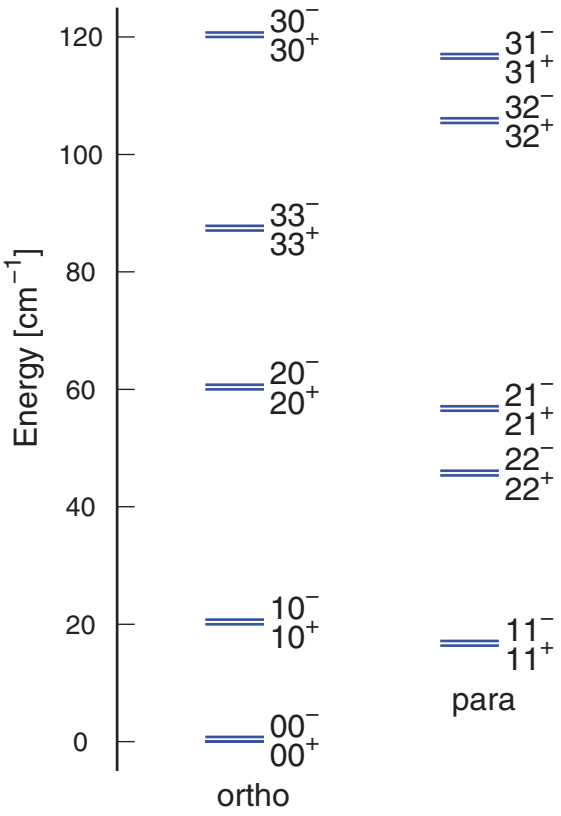

FIG. 1. Energy levels $|jk\pm\rangle$ of the ammonia molecule, where j is the angular momentum of the molecule, k is the projection on its threefold symmetry axis and $\pm$ refers to the symmetric/antisymmetric umbrella state. Throughout this article, we use the $|11-\rangle$ state as the initial state, so that we only consider *para* ammonia. We do not take into account hyperfine interactions. The collision energy is defined relative to the initial state.

II. THEORY

To theoretically study the low-energy scattering of NH_3 molecules with He atoms, we briefly introduce three coordinate frames that are used in the calculations.[30] These coordinate frames are discussed in more detail in the Appendix. The first frame is an orthonormal, right-handed space-fixed ("sf") laboratory frame located at the center of mass **Q** of the dimer. The coordinate R is the length of the vector **R** that points from the center of mass **X** of the NH_3 monomer to the He atom, while θ^{sf} is the zenith angle of the vector **R** and ϕ^{sf} is the azimuth angle in the space-fixed frame. The second frame is an orthonormal, right-handed body-fixed ("bf") dimer frame, also centered at the center of mass of the dimer. As explained in the Appendix, this frame is obtained by a rotation that aligns its z axis with the vector **R**. The third frame is an orthonormal, right-handed monomer-fixed ("mf") frame centered at the center of mass of the NH_3 molecule, whose z axis is aligned with the symmetry axis of the ammonia molecule. This monomer frame is obtained from the space-fixed frame by rotating over the three Euler angles $\zeta^{\text{sf}} = (\alpha^{\text{sf}}, \beta^{\text{sf}}, \gamma^{\text{sf}})$. Here, α^{sf} and β^{sf} are the azimuth and zenith angles of the ammonia C_3 symmetry axis in the space-fixed frame, while γ^{sf} describes the rotation of the NH_3 molecule about this axis. The Euler angles of the monomer frame can also be given with respect to the body-fixed frame, and are

then denoted by $\zeta^{\rm bf} = (\alpha^{\rm bf}, \beta^{\rm bf}, \gamma^{\rm bf})$. Finally, we introduce the umbrella or inversion angle ρ of the ammonia molecule, which is the angle between the z axis of the monomer frame and a vector pointing from the N atom to one of the H atoms, so that $\rho = \pi/2$ corresponds to a planar NH_3 geometry.

The Hamiltonian of the NH_3-He system can now be written as[31]

$$\hat{H} = \hat{H}_{\rm mol} - \frac{1}{2\mu R}\frac{\partial^2}{\partial R^2}R + \frac{1}{2\mu R^2}[\hat{J}^2 + \hat{j}^2 - 2\hat{\mathbf{j}}\cdot\hat{\mathbf{J}}] + V_{\rm int}(R, \beta^{\rm bf}, \gamma^{\rm bf}, \rho), \quad (1)$$

where throughout the article we set $\hbar = 1$, $\hat{H}_{\rm mol}$ is the Hamiltonian of the NH_3 molecule, μ is the reduced mass of the atom-molecule complex, $\hat{\mathbf{j}}$ is the angular momentum operator of the NH_3 monomer with respect to the body-fixed frame, $\hat{\mathbf{J}}$ is the total angular momentum operator also with respect to the body-fixed frame, and $V_{\rm int}$ is the interaction energy. We consider the interaction potential to depend on four coordinates, which implies that we assume the N-H bond length to be fixed and NH_3 to keep its threefold symmetry. The Hamiltonian of the NH_3 molecule includes the monomer's rotation, as well as the kinetic and potential energy of its umbrella motion,[31] namely,

$$\hat{H}_{\rm mol} = \sum_{\lambda=x,y,z}\frac{\hat{j}_\lambda^2}{2I_{\lambda\lambda}(\rho)} - \frac{1}{2\sqrt{g(\rho)}}\frac{\partial}{\partial\rho}\frac{\sqrt{g(\rho)}}{I_{\rho\rho}(\rho)}\frac{\partial}{\partial\rho} + V_{\rm umb}(\rho), \quad (2)$$

where $I_{xx}(\rho)$, $I_{yy}(\rho)$, and $I_{zz}(\rho)$ are the moments of inertia of the threefold symmetric ammonia molecule with respect to the monomer frame axes, see, e.g., Ref. 31, while $I_{\rho\rho}(\rho) = 3m_{\rm H}r_0^2(\cos^2\rho + \eta\sin^2\rho)$ with $m_{\rm H}$ the hydrogen mass, $r_0 = 1.9099a_0$, the fixed N-H bond length,[32] $\eta = m_{\rm N}/(3m_{\rm H} + m_{\rm N})$ and $m_{\rm N}$ the nitrogen mass. Moreover, we have that $g(\rho) = I_{xx}I_{yy}I_{zz}I_{\rho\rho}$, while the potential energy for the umbrella motion $V_{\rm umb}(\rho)$ leads to a double well potential that we model by

$$V_{\rm umb}(\rho) = \frac{k_\rho}{2}\left(\rho - \frac{\pi}{2}\right)^2 + a_\rho\exp\left[-b_\rho\left(\rho - \frac{\pi}{2}\right)^2\right], \quad (3)$$

with the parameters $k_\rho = 90\,651$ cm^{-1}rad^{-2}, $a_\rho = 23\,229$ cm^{-1}, and $b_\rho = 3.1846$ rad^{-2}. The resulting double well potential gives rise to umbrella vibration levels of which two levels have an energy below that of the barrier at the planar ammonia geometry.[31] Moreover, each of these two vibration levels splits into a pair of energy levels due to tunneling. The parameters of the umbrella potential are chosen such that the experimental energy splitting between the two tunnel states in the vibrational ground state, as well as the experimental splittings[33] between the ground state and the two tunnel states of the first vibrationally excited level are accurately reproduced.

To treat the Schrödinger equation in body-fixed coordinates, we expand the scattering wavefunction in the following coupled-channel basis

$$\Psi^{\rm bf}(R) = \frac{1}{R}\sum_{\mathbf{n}}|\mathbf{n}\rangle\chi_{\mathbf{n}}(R), \quad (4)$$

where the radial dependence of the wavefunction is given by $\chi_{\mathbf{n}}(R)$, while the body-fixed angular basis set,

$$|\mathbf{n}\rangle \equiv |j, k, K, J, M_J, v^{\pm}\rangle = \left[\frac{(2j+1)(2J+1)}{32\pi^3}\right]^{1/2} \times\phi_v^{\pm}(\rho)D_{Kk}^{(j)*}(\zeta^{\rm bf})D_{M_JK}^{(J)*}(\phi^{\rm sf}, \theta^{\rm sf}, 0), \quad (5)$$

is used to treat the angular part of the Hamiltonian. Here, $D_{mm'}^{(j)*}(\zeta) = e^{im\alpha}d_{mm'}^{(j)}(\beta)e^{im'\gamma}$ with $d_{mm'}^{(j)}(\beta)$ the well-known Wigner d-functions, k is the projection quantum number of the monomer angular momentum with eigenvalue j on the monomer z axis, K is the projection quantum number of both the monomer angular momentum and the total angular momentum with eigenvalue J on the body-fixed dimer z axis, M_J is the projection of the total angular momentum on the space-fixed z axis, v is the umbrella vibration quantum number, and the superscript $\pm$ refers to the even/odd umbrella tunneling function.

As a result, our task is to solve the following second-order matrix differential equation:

$$-\frac{\partial^2\chi_{\mathbf{n}'}(R)}{\partial R^2} = \sum_{\mathbf{n}}\langle\mathbf{n}'|\hat{W}|\mathbf{n}\rangle\chi_{\mathbf{n}}(R), \quad (6)$$

where we introduced the operator $\hat{W} = 2\mu(E - \hat{H} + \hat{K})$ with the kinetic energy operator $\hat{K}$ given by the second term on the right-hand side of Eq. (1). We note that J and M_J are good quantum numbers, and that the operator $\hat{W}$ is diagonal in J and independent of M_J. Furthermore, the monomer part of the Hamiltonian, $\hat{H}_{\rm mol}$, is also diagonal in the angular basis set. The complexity of the matrix $\langle\mathbf{n}'|\hat{W}|\mathbf{n}\rangle$ can be further reduced by considering the symmetry properties of the NH_3-He complex. Because the Hamiltonian commutes with permutations of the three hydrogen atoms in NH_3 and the operator for inversion in space $\hat{E}^*$, it is useful to adapt the basis states such that they transform as the irreducible representations of the corresponding molecular symmetry group D_{3h}(M) in the notation of Bunker and Jensen.[34] The adapted basis states of different symmetry cannot be mixed by the Hamiltonian. The precise procedure for this adaptation is described in the Appendix. Moreover, in Ref. 14, several useful relations can be found for determining the matrix elements of the $\hat{W}$ operator in the angular basis.

In order to fully solve Eq. (6), the wavefunctions must satisfy the appropriate scattering boundary conditions.[35] These boundary conditions are directly formulated in a space-fixed frame. The exact solution of the space-fixed Schrödinger equation at larger separations R, i.e., when the interaction energy has approached zero, is a linear combination of the proper spherical Bessel functions. These Bessel functions are labelled by the space-fixed end-over-end rotational quantum number L, which has become a good quantum number at such large separations. Therefore, the matching of the propagated wavefunction from Eq. (6) to spherical Bessel functions can be performed at distances where the centrifugal energy, set by L and decaying as R^{-2}, is still large, as long as the interaction energy, decaying in our case as R^{-6}, has become negligibly small. To perform the matching, it is necessary to transform between the body-fixed and the space-fixed basis sets. The

latter basis set is for the present case given by

$$|j,k,L,J,M_J,v^{\pm}\rangle = \left[\frac{(2j+1)(2L+1)}{32\pi^3}\right]^{1/2}\phi_v^{\pm}(\rho) \times \sum_{m_j,M_L} D^{(j)*}_{m_jk}(\zeta^{\rm sf})C^L_{M_L}(\theta^{\rm sf},\phi^{\rm sf}) \times \langle jm_j;LM_L|JM_J\rangle, \quad (7)$$

with $C^L_{M_L}(\theta^{\rm sf},\phi^{\rm sf})$ the Racah-normalized spherical harmonics and M_L the projection of the end-over-end angular momentum on the space-fixed z axis, m_j the projection of the monomer angular momentum on the space-fixed z axis, and $\langle j_1m_1;j_2m_2|j_3m_3\rangle$ a Clebsch–Gordan coefficient. The transformation between the body-fixed and the space-fixed basis then becomes[14]

$$|j,k,L,J,M_J,v^{\pm}\rangle = \sum_K |j,k,K,J,M_J,v^{\pm}\rangle\left(\frac{2L+1}{2J+1}\right)^{1/2} \times \langle jK;L0|JK\rangle. \quad (8)$$

To end our discussion of the matching procedure, we mention the various possible open and closed channels following from the Hamiltonian of Eq. (2). The vibration-tunneling states of the umbrella motion are determined by calculating the eigenstates of the Hamiltonian formed by the last two terms of Eq. (2). Only the lowest four eigenstates, labeled $\phi_v^{\pm}(\rho)$ with vibrational quantum numbers $v=0$ and $v=1$, are kept. With these four states as a basis for the umbrella motion, we turn to the first term of the Hamiltonian of Eq. (2). As a result, the rotational constants $1/2I_{\lambda\lambda}(\rho)$ become 4×4 matrices, but the $+$ and $-$ states are not mixed. The eigenstates that result from diagonalization of the full monomer Hamiltonian in a basis containing all rotational states with $j\le6$ and the four umbrella states, determine the open and closed channels. We label the open channels by $|jk\pm\rangle$; the vibrational quantum number v is omitted from this notation because all vibrational states with $v>0$ are closed for the energy range in which we are interested. We consider the ammonia molecules to be prepared in the $|11-\rangle$ state, so that the lower lying $|11+\rangle$ state is open for all collision energies. Increasing the collision energy beyond the energy of excited monomer states opens up the corresponding channels, and inelastic scattering into these states occurs if it is allowed by symmetry. The matching procedure of the wavefunctions to the boundary conditions for scattering at large distance R ultimately leads to an expression for the scattering matrix. This S matrix is subsequently directly related to the differential and integral cross sections for the elastic and inelastic channels, which can be compared with the outcome of collision experiments.[36]

III. THE NH_3-HE POTENTIAL

Before we can apply the above described formalism to solve the scattering problem, we need to determine the NH_3-He interaction potential. To this end *ab initio* calculations were performed with MOLPRO (Ref. 37) using the supermolecule approach with the counterpoise procedure of Boys and Bernardi.[38] We considered the interaction energy to be dependent on four coordinates, namely, R, $\beta^{\rm bf}$, $\gamma^{\rm bf}$, and ρ.

TABLE I. Comparison of the interaction energy between the CCSD(T) method (abbreviated as CC) and the CCSD(T)-F12 method (abbreviated as F12) for different basis sets and different geometries as calculated with MOLPRO (Ref. 37). We used the augmented triple zeta (AVTZ), quadruple zeta (AVQZ), and quintuple zeta (AV5Z) basis sets. We also studied the effect of midbond functions,[43] which are indicated in the table by the + sign, when they are added to the basis set. For the short-range geometry, indicated by $\mathbf{x}_{\rm s}$ in the table, we used $R=4.5a_0$, $\beta^{\rm sf}=0$, $\gamma^{\rm sf}=0$, and $\rho=14\pi/24$. For the mid-range geometry, indicated by $\mathbf{x}_{\rm m}$, we used $R=7a_0$, $\beta^{\rm sf}=\pi/2$, $\gamma^{\rm sf}=\pi/6$, and $\rho=15\pi/24$. For the long-range geometry, indicated by $\mathbf{x}_{\rm l}$, we used $R=15a_0$, $\beta^{\rm sf}=\pi$, $\gamma^{\rm sf}=\pi/3$ and $\rho=16\pi/24$. The interaction energies are given in $\rm cm^{-1}$.

	AVTZ	AVTZ+	AVQZ	AVQZ+	AV5Z
CC ($\mathbf{x}_{\rm s}$)	1446.2	1414.2	1407.4	1397.3	1394.7
F12 ($\mathbf{x}_{\rm s}$)	1393.5	1386.0	1389.8	1386.8	1386.1
CC ($\mathbf{x}_{\rm m}$)	−21.716	−23.529	−22.733	−23.521	−23.179
F12 ($\mathbf{x}_{\rm m}$)	−23.329	−23.679	−23.237	−23.510	−23.381
CC ($\mathbf{x}_{\rm l}$)	−0.2506	−0.2583	−0.2521	−0.2538	−0.2526
F12 ($\mathbf{x}_{\rm l}$)	−0.2622	−0.2637	−0.2548	−0.2554	−0.2524

The grid for the *ab initio* calculations consisted of 4180 points. For R, in total 19 points were used. In the short and intermediate range, i.e., for $4a_0\le R\le10a_0$, we used an equidistant grid of 13 points with a separation of $0.5a_0$, while in the long range, that is for $R>10a_0$, we used an approximately logarithmic grid consisting of the points $12a_0$, $14.4a_0$, $17.3a_0$, $20.8a_0$, $25a_0$, and $30a_0$. For $\beta^{\rm bf}$, we used a Gauss–Legendre grid consisting of 11 points for $0\le\beta^{\rm bf}\le\pi$, while for $\gamma^{\rm bf}$, we used an equidistant Gauss–Chebyshev grid consisting of the points $\pi/24$, $3\pi/24$, $5\pi/24$, and $7\pi/24$. Finally, for the grid in ρ we used an equidistant grid of 5 points, where the middle point was given by the value $\rho_3=0.6226\pi$, while the distance between the points was given by $\Delta\rho=(2\rho_3-\pi)/5$.

The calculations in the long range were performed with the coupled-cluster method taking into account single and double excitations and a perturbative treatment of triple excitations [CCSD(T)] (Ref. 39) using the augmented correlation-consistent polarized valence quadruple-zeta (AVQZ) basis set.[40,41] For the short range, we used the explicitly correlated CCSD(T)-F12 method[42] to account more efficiently for the strong effect of electron correlations in this regime. The CCSD(T)-F12 method was found to yield accurate results with the smaller triple-zeta basis set (AVTZ), as illustrated by Table I. In this table, the interaction energies are shown for different NH_3-He geometries in the short, intermediate, and long range with both the CCSD(T) and the CCSD(T)-F12 method using different basis sets. Also the effect of using midbond functions[43] is included in this table, where the midbond orbitals were located along the vector connecting the center of mass of the ammonia molecule with the helium atom at a distance of $(r_0+R)/2$ from the ammonia center of mass. Particularly in the short and intermediate range, these midbond functions improve the interaction energies, so that they were used in the calculations with F12. From Table I, we see that in the short range, the CCSD(T)-F12 method with an AVTZ basis set including midbond functions performs better than the CCSD(T) method with an AV5Z basis set, although the latter calculation is much more expensive due to the large basis set.

The main reason why we did not use the F12 method in the long range is that we found that the implementation of this method in MOLPRO (Ref. 37) gives rise to an incorrect $1/R$ behavior in the very long range, rather than the correct $1/R^6$ behavior for the system under consideration. This behavior is caused by the fitting of the electron density distributions, which unfortunately does not result in exactly charge neutral monomers. Although the artificial residual charges can be reduced by introducing a larger electron density fitting basis set, the $1/R$ behavior will eventually always dominate the correct $1/R^6$ behavior. Hence, we decided to use the CCSD(T) method without F12 for the long range. We used the AVQZ basis set, and we may conclude from Table I that this basis set indeed gives rise to accurate interaction energies in the long range. In order to switch smoothly between the results of the two methods, we used the switching function $s(R)$,

$$s(R) = \begin{cases} 0 & \text{if} \quad R \le a \\ 1 & \text{if} \quad R \ge b \\ \frac{1}{2} + \frac{1}{4}\sin\frac{\pi x}{2}(3 - \sin^2\frac{\pi x}{2}) & \text{otherwise,} \end{cases} \tag{9}$$

with $x = (2R - b - a)/(b - a)$, $a = 10a_0$, and $b = 13a_0$. The function is chosen such that the first three derivatives of s at $R = a$ and $R = b$ are zero. We thus calculated the interaction energies for the angular geometries at distance $R = 12a_0$ with both methods, where the calculated value with F12 was given a weight of $1 - s(12a_0)$, while the value without F12 was given a weight $s(12a_0)$.

To obtain an analytic representation of the interaction potential between the NH_3 molecules and the He atoms, we first perform an expansion in tesseral spherical harmonics, namely,

$$V_{\text{int}}(R, \beta^{\text{bf}}, \gamma^{\text{bf}}, \rho) = \sum_{l,m}(-1)^m v_{lm}(R, \rho) S_{lm}(\beta^{\text{bf}}, \gamma^{\text{bf}}), \tag{10}$$

where due to the symmetry of the dimer only terms with $m = 0, 3, 6, \ldots$ are present. Because we have 11 grid points in β^{bf}, the summation over l is from $0 \le l \le 10$. The summation over m is from 0 to the largest multiple of 3 that is smaller than or equal to the corresponding l value. On all grid points R_i and ρ_j, we determine the coefficients of the angular expansion $v_{lm}(R_i, \rho_j)$ by means of a quadrature on the *ab initio* grid with the appropriate Gauss–Legendre and Gauss–Chebyshev weights.[14] For the resulting expansion coefficients v_{lm}, we distinguish between the short-range and the long-range behavior, so that $v_{lm}(R, \rho) = v^{\text{sr}}_{lm}(R, \rho) + v^{\text{lr}}_{lm}(R, \rho)$. Both in the short range and the long range, the dependence of the coefficients v_{lm} on ρ is represented by a polynomial expansion in $(\rho - \pi/2)^p$, where p ranges from 0 to 9. If $l + m$ is even, then the polynomial expansion only contains even powers in p, while if $l + m$ is odd only odd powers are present. In the long range, we expanded the potential in powers of R^{-n}, resulting in

$$v^{\text{lr}}_{lm}(R, \rho) = \sum_{n,p} c_{lmpn} f_n(aR) \left(\rho - \frac{\pi}{2}\right)^p R^{-n}, \tag{11}$$

where the inverse powers of R that are involved depend on l. It can be shown[44] that for $l = 0, 2$ the expansion starts with $n_i = 6$, while for $l = 1, 3$ it starts with $n_i = 7$. For $l \ge 4$, it starts with $n_i = l + 4$. We used the analytic long range expansion of Eq. (11) only for $l \le 5$, and for each l we took the leading term R^{-n_i} and the next-to-leading term R^{-n_i-2} into account. The Tang–Toennies damping function

$$f_n(x) = 1 - \left(\sum_{i=0}^{n} \frac{x^i}{i!}\right) e^{-x}, \tag{12}$$

was included to avoid the singular behavior of the long-range terms in the short range.[45] For the value of a in Eq. (11), we used the isotropic exponent in the short-range, or, to be more precise, $a = \ln[v_{00}(R_1, \rho_3)/v_{00}(R_2, \rho_3)]/\Delta R = 2.088a_0^{-1}$ with R_1 and R_2 the first two points of the R grid and $\Delta R = R_2 - R_1$. The expansion coefficients c_{lmpn} were obtained from $v_{lm}(R_i, \rho_j)$ by performing a weighted least-squares fit using the last three points of the R grid and all points of the ρ grid. The three R points were weighted for each l by $R_i^{n_i}$, with n_i the leading power of the long range decay for the considered l.

To describe the short and intermediate range of the potential the same expansion was employed in β^{bf}, γ^{bf}, and ρ as for the long range, but the behavior in R was treated differently. The following procedure was used. First, for all the grid geometries, the corresponding value of the analytic long range potential was subtracted from the *ab initio* values. Next, after performing the expansion in tesseral harmonics and powers of $(\rho - \pi/2)$, the behavior of the resulting coefficients $v_{lmp}(R)$ was interpolated with a reproducing kernel Hilbert space (RKHS) method.[46] The smoothness parameter of the RKHS interpolation was set to 2, while the RKHS parameter m_{RKHS}, which determines the power with which the interpolation function decays, was chosen to depend on l. For $l \le 5$, the parameter was set to $m_{\text{RKHS}} = n_i + 1$. Then the RKHS function decays as R^{-n_i-2}, which is faster for each l than the leading term in the analytic fit of Eq. (11). However, for $l > 5$, no analytic long range fit was done, and we used $m_{\text{RKHS}} = n_i - 1$. As a result, the corresponding RKHS functions decayed for each l as R^{-n_i} with $n_i = l + 4$, which is the correct leading long range behavior for $l > 5$.[44]

We have compared the fitted potential with the *ab initio* values on the full grid to test the accuracy of the fit in the angles β^{bf}, γ^{bf}, and ρ. The quality of the fit in R cannot be tested in this way, because the RKHS procedure goes by construction precisely through the points to be fitted. We calculated the RMS (root mean square) error for each grid distance R_i and divided by the mean *ab initio* interaction energy at that distance, giving for the relative RMS error $\xi(R_i)$ that

$$\xi(R_i) = \frac{\sqrt{\frac{1}{n}\sum_{j,k,l}[\Delta V(R_i, \beta^{\text{bf}}_j, \gamma^{\text{bf}}_k, \rho_l)]^2}}{\left|\frac{1}{n}\sum_{j,k,l} V^{\text{abi}}_{\text{int}}(R_i, \beta^{\text{bf}}_j, \gamma^{\text{bf}}_k, \rho_l)\right|} 100\%, \tag{13}$$

where $\Delta V(R_i, \beta^{\text{bf}}_j, \gamma^{\text{bf}}_k, \rho_l) = V^{\text{fit}}_{\text{int}}(R_i, \beta^{\text{bf}}_j, \gamma^{\text{bf}}_k, \rho_l) - V^{\text{abi}}_{\text{int}}(R_i, \beta^{\text{bf}}_j, \gamma^{\text{bf}}_k, \rho_l)$, and the summations are over all $n = 220$ angular grid points. For our potential fit, we found that the relative error $\xi(R_i)$ is less than 0.05 % for all R_i, so the fits in the angular coordinates are excellent. To also test the fit in R, we calculated *ab initio* interaction energies for an additional 495 points, that were chosen to lie about halfway between

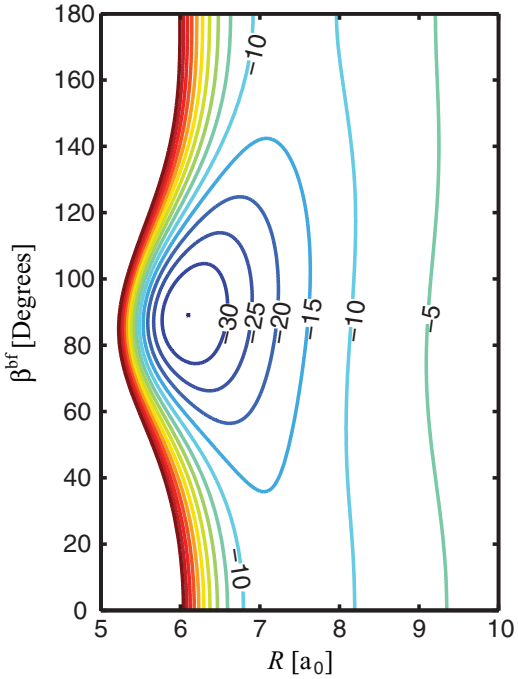

FIG. 2. Contour plot of the NH_3-He interaction potential as a function of R and β^{bf} for $\gamma^{bf} = 0$ and the equilibrium umbrella angle $\rho_e = 112.15°$. The energies of the contours are given in cm^{-1}.

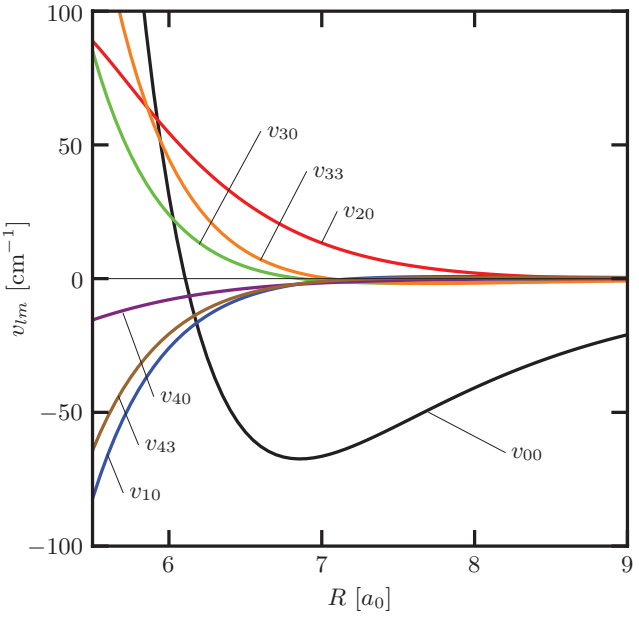

FIG. 3. Coefficients $v_{lm}(R, \rho_e)$ of the NH_3-He interaction energy as a function of center of mass distance R, evaluated at the equilibrium umbrella angle $\rho_e = 112.15°$. The isotropic $v_{00}(R, \rho_e)$ coefficient is largest. The v_{10}, v_{20}, v_{30}, v_{33}, v_{40}, and v_{43} coefficients are shown as well.

the grid points used for the fit. The relative RMS error of the values calculated from the fit compared to the new *ab initio* values depended quite strongly on R, where the largest error was found to occur in the short range. Namely, for the test points at $R = 4.3a_0$, we found with the use of 45 different angular points a relative RMS error of 3.5%, while for all other R values we obtained a relative error of about 0.5% or less. An important reason for this behavior is that we use a RKHS fit for the short range, which behaves as a power law, while the true behavior of the potential is exponential. The fitting procedure could thus have been further improved using an exponential form. However, we note that already the present fitting error is rather small. Moreover, in the present paper, we use the potential to describe cold scattering with collision energies of maximally 130 cm^{-1}, so that the extreme short-range behavior of the potential is not being probed.

In Fig. 2, we show a contour plot of the NH_3-He interaction potential for $\gamma^{bf} = 0$ and the equilibrium umbrella angle $\rho_e = 112.15°$. For this value of γ^{bf} and ρ, the minimum of the potential is given by $V_{min} = -35.08$ cm^{-1} for $R = 6.095$ a_0 and $\beta^{bf} = 89.0°$. This may be compared to the potential of Hodges and Wheatley,[29] where the minimum of the potential for $\gamma^{bf} = 0$ and $\rho_e = 112.15°$ is given by $V_{min} = -33.46$ cm^{-1} for $R = 6.133$ a_0 and $\beta^{bf} = 88.75°$. Although this difference in the well depth is not very large, we have found that the consequences for low-energy scattering can still be quite substantial, as we will discuss in Sec. V. Finally, we have for the leading isotropic coefficient, defined as $C_6 = -v_{00}(R, \rho_3)R^6$ for large R, that in atomic units $C_6 = 39.6E_h a_0^6$. The relative importance of the various $v_{lm}(R, \rho_e)$ expansion coefficients is shown in Fig. 3. The potential is available in FORTRAN 77 online (see supplemental material given in Ref. 47).

IV. COMPUTATIONAL ASPECTS

Having discussed the formalism and the potential, we now turn to the numerical procedures that we used in order to obtain converged cross sections that can be compared with future cold-collision experiments. To numerically determine the four lowest lying vibration-inversion levels $\phi_v^{\pm}(\rho)$ of the Hamiltonian of Eq. (2) for $j = 0$, we used the discrete variable representation based on sinc-functions (sinc-DVR).[48] The resulting eigenfunctions were used to determine the matrix elements $\langle\phi'|1/2I_{\lambda\lambda}|\phi\rangle$ with $\phi = \phi_v^{\pm}(\rho)$ by numerical integration. For the propagation in solving Eq. (6), the renormalized Numerov algorithm was used, starting at $4a_0$ and ending at $50a_0$, using an equidistant grid with 273 points. The renormalized Numerov method also allows for a complete reconstruction of the scattering wavefunctions.

The angular basis set contained all monomer states with $j \leq 6$, where we checked that the inclusion of more monomer levels resulted only in deviations of maximally 1 % for the calculated cross sections. The maximal value for the total angular momentum J that we used depended on the collision energy. For collision energies $E \leq 10$ cm^{-1}, we included all angular basis states with $J \leq 10$, while for $10 < E \leq 50$ cm^{-1}, we included all basis states with $J \leq 20$, and for $50 < E \leq 130$ cm^{-1}, we included all states with $J \leq 30$. The convergence of the cross sections with respect to the total angular momentum J is slowest for the elastic cross section. The inelastic cross sections are converged at considerably lower values of J than reported here.

In order to check our results and gain additional insight, we also implemented a commonly applied model to treat the ammonia umbrella motion in scattering calculations.[49,50] In this model, no vibrationally excited umbrella states are taken into account and the ground-state umbrella tunneling states

are approximated as an even and odd combination of the two rigid equilibrium structures. These two states are thus written as $|\pm\rangle = [f(\rho - \rho_e) \pm f(\pi - \rho + \rho_e)]/2^{1/2}$, where $f(x)$ is a function localized around $x = 0$. More precisely, the two-state model amounts to approximating the matrix elements of the potential by $\langle\pm|v_{lm}(R, \rho)|\pm\rangle = v_{lm}(R, \rho_e)$ for $l + m$ even, and $\langle\pm|v_{lm}(R, \rho)|\mp\rangle = v_{lm}(R, \rho_e)$ for $l + m$ odd. For the rotational constants, we use the experimentally determined values $A_{xx} = A_{yy} = 9.9402$ cm^{-1}, and $A_{zz} = 6.3044$ cm^{-1} in the model. Furthermore, we include the experimental ground state splitting of 0.79 cm^{-1} (Ref. 33) between the two tunneling states in the scattering calculations. This simple model has been implemented in the scattering program MOLSCAT.[51] We have used MOLSCAT to double-check the results that we obtained from our own scattering program. The model was previously found to result in good agreement with more elaborate treatments of the umbrella motion for scattering at higher collision energies.[52] In this article, we also want to test the accuracy of the model for cold collisions, and in particular for the calculation of scattering resonances.

V. RESULTS

In Fig. 4, we show the integral cross sections for the scattering of NH_3 molecules with He atoms for collision energies ranging from 10^{-4} cm^{-1} to 20 cm^{-1}. Initially, we only have elastic scattering and inelastic scattering into the $|11+\rangle$ state, which lies 0.79 cm^{-1} lower in energy. Figure 4 was made using the previously described elaborate treatment of the umbrella motion; however, with the use of the model treatment almost exactly the same results were obtained. We observe in the first place that, in agreement with the Wigner threshold laws,[53] the elastic cross section becomes constant for very small collision energies, while the inelastic cross section decreases with E as $1/\sqrt{E}$. Going more into the details of the figure, we observe two shape resonances closely together in the elastic channel at collision energies of 1.86 and 2.22 cm^{-1}.

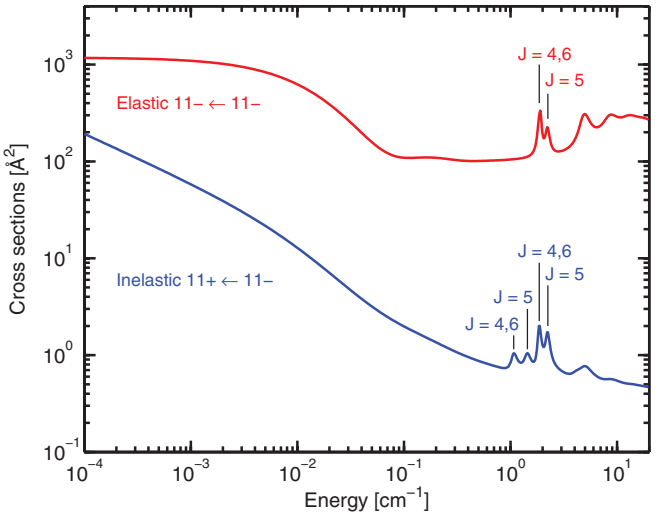

FIG. 4. Integral cross sections for NH_3-He scattering as a function of collision energy. The initial state of the NH_3 molecule is the $|11-\rangle$ state. At low collision energies only elastic scattering (upper red curve) and inelastic scattering into the lower lying $|11+\rangle$ state (lower blue curve) can occur.

In bound state calculations with the NH_3-He complex enclosed in a box of variable size, we found continuum levels with nearly the same energies that are practically independent of the box size, so we may conclude that these peaks in the scattering cross section indeed correspond to shape or orbiting resonances caused by quasi-bound states. Such quasi-bound states may occur either in the incoming or in the outgoing scattering channel; for the specific case of elastic scattering, these are the same. Looking at the dominant contributions to the cross section, the first peak was found to be mainly caused by quasi-bound states with total angular momenta $J = 4$ and $J = 6$, while the second peak was mainly caused by a quasi-bound state with total angular momentum $J = 5$. In both cases, they corresponded to an end-over-end angular momentum of $L = 5$. Looking in the same energy range at the inelastic scattering into the $|11+\rangle$ state, we observe not only two similar peaks at the same collision energies, but also two additional peaks at 1.08 and 1.44 cm^{-1}. These two additional shape resonances can be readily understood by noting that for inelastic scattering the resonant quasi-bound state can occur either in the incoming channel or in the outgoing channel, where the latter channel is about 0.8 cm^{-1} lower in energy. This is indeed precisely the energy with which the two additional peaks in the inelastic channel are shifted to the left in Fig. 4.

For completeness, we note that we studied this collision energy range also with the potential of Hodges and Wheatley.[29] Although the difference in the well depth between the two potentials at the equilibrium umbrella angle was only about 5%, we still found large differences in the resonant structures at very low energies. For example, using the Hodges and Wheatley potential,[29] we observed two very strong shape resonances at collision energies of 0.03 and 0.45 cm^{-1} induced by quasi-bound states with total angular momenta $J = 3$ and $J = 4$ and end-over-end angular momentum $L = 4$. However, because our own potential is deeper, we find that these quasi-bound states have become true bound states with energies below the scattering continuum, so that they cannot cause shape resonances anymore. As a result, the first shape resonances we find with our potential are induced by quasi-bound states with total angular momenta $J = 4$, 5, and 6 and $L = 5$, as shown in Fig. 4. This point also clearly shows that scattering resonances at low energy can be very sensitive to the precise shape of the potential energy surface, which means that accurate scattering experiments can be used to probe very precisely our knowledge of intermolecular interactions.

In Fig. 5, we again show the integral cross sections for elastic scattering and inelastic scattering into the $|11+\rangle$ state, but now considering collision energies from 10 to 50 cm^{-1}. Note that the inelastic cross is actually 150 times smaller than shown in the figure. As can be seen from Fig. 1, at a collision energy of 28.33 cm^{-1}, it becomes energetically possible to excite the ammonia molecule from its $|11-\rangle$ state to its $|22+\rangle$ state, and a new scattering channel opens. At 29.12, 39.33, and 40.12 cm^{-1}, the $|22-\rangle$, $|21+\rangle$, and $|21-\rangle$ channels open, respectively, as also indicated in Fig. 5. The opening of the new channels is seen to have a profound effect on the inelastic cross sections to the $|11+\rangle$ state. Namely, before these new channels open a bunch of Feshbach resonances is observed.

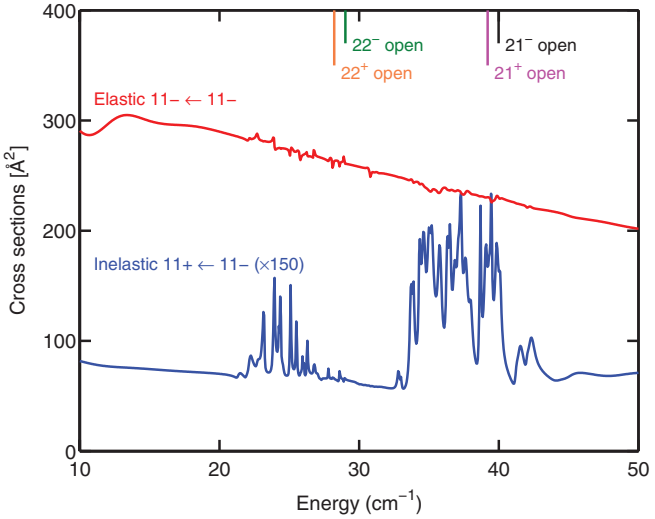

FIG. 5. Elastic (upper red curve) and inversion inelastic (lower blue curve) integral cross sections as a function of collision energy for NH_3-He scattering. The inelastic cross section is scaled with a factor of 150, so that the actual inelastic cross section is 150 times smaller than shown in the figure. At higher collision energies, the $|22\pm\rangle$ and the $|21\pm\rangle$ channels open. As a result, Feshbach resonances are observed, which are most pronounced for the inelastic scattering into the $|11+\rangle$ state.

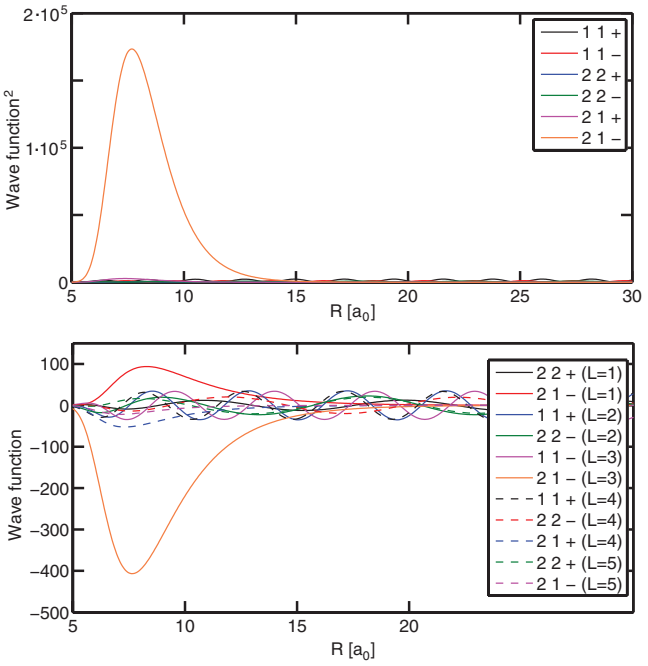

FIG. 6. Bottom panel: Contributions of various channels and partial waves to the scattering wavefunction at a collision energy of 37.28 cm^{-1}, where a Feshbach resonance for inelastic scattering into the $|11+\rangle$ state occurs. We used a total angular momentum of $J = 3$ and considered E'' symmetry. As a result, the initial state $|11-\rangle$ asymptotically corresponds to $L = 3$, while there are eight open partial waves in outgoing channels. The wavefunctions are flux normalized and are given in atomic units. Top panel: Contributions of various channels to the square of the wavefunction. In the inner region, where the collision takes place, a large amplitude in the asymptotically closed $|21-\rangle$ channel is observed.

These resonant structures are called Feshbach resonances because they are caused by a molecular level that is different from the incoming and the outgoing channel. In Fig. 5, we see that especially the Feshbach resonances induced by the $|21\pm\rangle$ levels at collision energies around 40 cm^{-1} are strong, giving rise to almost a factor of 3 increase compared to the background inelastic cross section. These resonances seem to be particularly suited to observation in a collision experiment. We come back to this point more elaborately in Sec. VI.

To understand the Feshbach resonances in more detail, we have studied the scattering wavefunctions. In Fig. 6, contributions to the scattering wavefunction are shown at a collision energy of 37.28 cm^{-1}. At this collision energy, there is a Feshbach resonance for inelastic scattering into the $|11+\rangle$ state, somewhat below the energy at which the $|21-\rangle$ channel opens. In the bottom panel of Fig. 6, we show contributions of different open and closed channels to the scattering wavefunction. For this particular figure, we considered a total angular momentum of $J = 3$ and symmetry E'' (see the Appendix). This means that for the incoming channel, i.e., the $|11-\rangle$ state, asymptotically only the partial wave with $L = 3$ contributed. For the four open outgoing channels, namely $|11\pm\rangle$ and $|22\pm\rangle$, in total eight open partial waves are possible for the considered J and E'' symmetry. In the inner region also contributions corresponding to asymptotically closed channels can gain amplitude, when they are coupled to the considered incoming state and outgoing state by the interaction potential. In the top panel of Fig. 6, we show for each channel the resulting contributions to the square of the wavefunction. From Fig. 6, we clearly see that in particular the closed $|21-\rangle$ channel has a very strong amplitude in the collision region, which shows that this state is responsible for the strong Feshbach resonance observed at this collision energy.

A different way to study the Feshbach resonances is by looking at phase shifts in the scattering wavefunction. These phase shifts can be obtained from the eigenvalues of the scattering matrix.[36,54] In Fig. 7, we show in the top panel the sums of the phase shifts in all open channels for various total angular momenta J. Since we consider both symmetries E' and E'', we have two curves for each J. From scattering theory it follows that when a resonance occurs, the phase shift sum rapidly increases by π as a function of energy.[54] In the top panel of Fig. 7, we indeed see this happening many times at the collision energies where resonances are found in the elastic and inelastic cross sections. The derivatives of the phase shifts with respect to the energy give the lifetimes of the collision complexes.[36] These lifetimes are shown in the lower panel of Fig. 7. This figure shows that at the collision energies where resonances occur, we indeed have long-lived intermediate quasi-bound states.

In Fig. 8, we show the integral cross sections for inelastic scattering into the $|21\pm\rangle$ and the $|22\pm\rangle$ states, for a collision energy ranging from the energies at which these channels open, up to 50 cm^{-1}. Note that the inelastic cross sections to the $|22+\rangle$ and $|21+\rangle$ states are scaled with a factor of 2. Immediately after each channel opens, we see strong resonant features, which are shape resonances, caused by quasi-bound states in the outgoing channel. In the $|22\pm\rangle$ channels, we also find Feshbach resonances due to quasi-bound states of $|21\pm\rangle$ character.

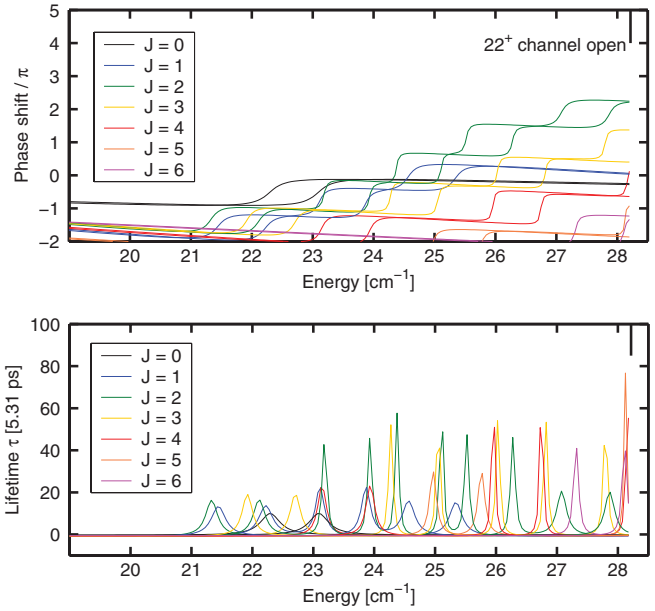

FIG. 7. Top panel: Phase shift sum as a function of collision energy for various total angular momenta J. Both E' and E'' symmetries are considered, so that we have two curves for each J. Bottom panel: The corresponding lifetimes as a function of the collision energy. The lifetimes are obtained from the derivative of the phase shifts with respect to the collision energy (in cm^{-1}); they are given in units of 5.3088 ps.

In the energy range from 10 to 50 cm^{-1}, we also studied the scattering cross sections using the previously described model treatment of the NH_3 umbrella motion. We found that the model calculations have the tendency to somewhat overestimate the strength of certain resonance peaks compared to the elaborate treatment of the umbrella motion. Studying this effect in more detail, we found that the differences are mainly due to the approximation of the nonzero potential matrix elements for the two tunneling states as $v_{lm}(R, \rho_e)$, rather than due to the neglect of the higher lying $\phi_1^{\pm}(\rho)$ states. Namely,

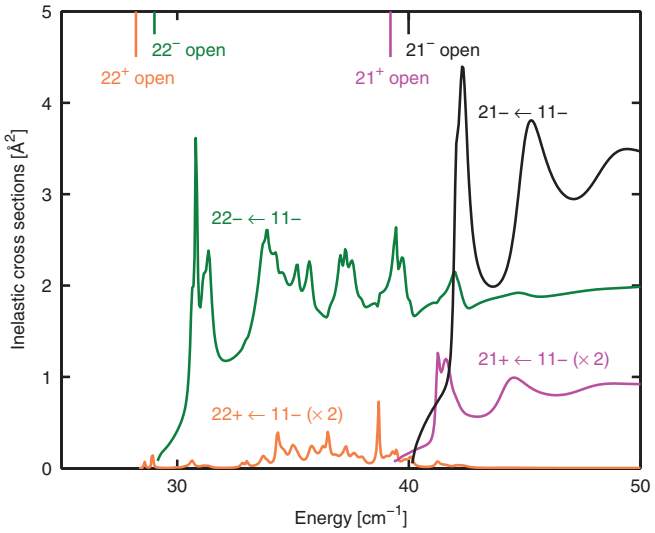

FIG. 8. Inelastic integral cross sections for scattering into the $|22\pm\rangle$ channels and the $|21\pm\rangle$ channels as a function of collision energy. The inelastic cross sections for the $|22+\rangle$ and the $|21+\rangle$ channels are scaled with a factor of 2. After the various channels open, shape resonances are observed.

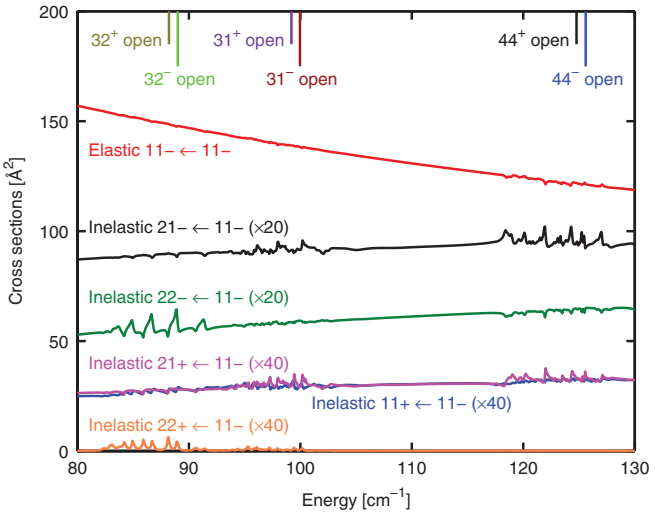

FIG. 9. Elastic and inelastic integral cross sections for scattering into the $|11+\rangle$, $|22\pm\rangle$, and $|21\pm\rangle$ states as a function of collision energy. The inelastic cross sections for the $|22-\rangle$ and $|21-\rangle$ channels are scaled with a factor of 20, and for the $|11+\rangle$, $|22+\rangle$, and $|21+\rangle$ channels with a factor of 40. At higher collision energies, various $|3k\pm\rangle$ and $|4k\pm\rangle$ channels for the *para* ammonia molecules open. As a result, small Feshbach resonances are observed.

by calculating the cross sections with the elaborate treatment and taking only the lowest two umbrella functions $\phi_0^{\pm}(\rho)$ into account we obtained cross sections that were nearly equal to the elaborate treatment with four umbrella functions, while they gave rise to the same differences with the model treatment. However, we note that in general the model treatment performed very satisfactory in describing the resonance structures. All resonant peaks found with the elaborate treatment were also found with the model treatment, and typically the strength of the scattering resonances differed by less than 10%. Because the precise strength and location of the resonances are very sensitive to the the potential, we conclude that the use of the model treatment is useful in studying scattering resonances, especially in cases when the elaborate treatment is computationally too expensive.

Looking again at Fig. 8, we note that there are significant differences in the magnitudes of the inelastic cross sections for the various collision channels. For example, the transition to the $|22-\rangle$ state is seen to be much stronger than the transition to the $|22+\rangle$ state, and the same holds for the transition to the $|21-\rangle$ state compared to the $|21+\rangle$ state. The relative magnitude of the integral cross sections for the elastic and inelastic scattering channels can be even more clearly observed in Fig. 9. In this figure, we show the integral cross sections for scattering into the $|11\pm\rangle$, $|21\pm\rangle$, and $|22\pm\rangle$ states, for collision energies ranging from 80 cm^{-1} to 130 cm^{-1}. Notice the scaling of the inelastic cross sections indicated in the figure. To explain the relative strengths of the transitions shown, we note that the scattering from the $|11-\rangle$ channel into different $|jk\pm\rangle$ channels is caused by different anisotropic terms in the interaction potential with coefficients $v_{lm}(R, \rho)$, cf. Eq. (10). For example, in order to change the umbrella state of the ammonia molecule (i.e., going from the odd $-$ state to the even $+$ state) we need terms in the potential for which $l + m$ is odd, so that also the corresponding coefficient $v_{lm}(R, \rho)$ is odd in

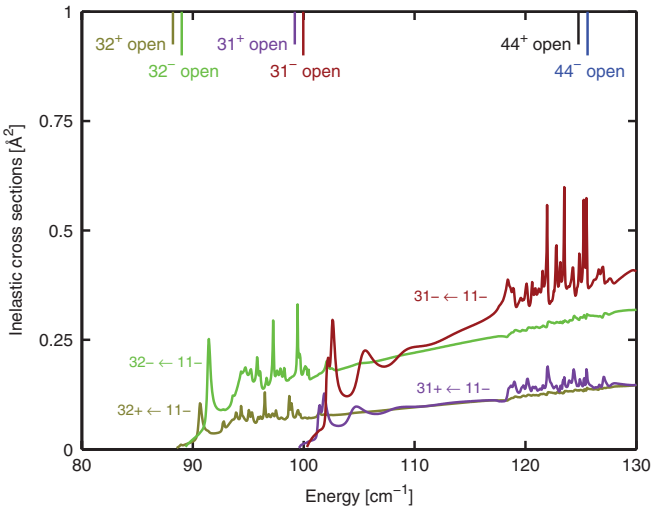

FIG. 10. Inelastic integral cross sections for scattering into the $|32\pm\rangle$ and the $|31\pm\rangle$ states as a function of collision energy. At higher collision energies, the $|44\pm\rangle$ channels for the *para* ammonia molecules open. As a result, Feshbach resonances are observed.

ρ. The various potential energy coefficients are plotted as a function of R at the equilibrium umbrella angle ρ_e in Fig. 3.

From this figure, we see that the isotropic coefficient $v_{00}(R, \rho_e)$ is by far the largest coefficient of all. This coefficient can only couple the initial $|11-\rangle$ state to itself (see for example Refs. 14 and 55), causing a large elastic scattering cross section. For a transition to a different umbrella state, or to a state with different j, we need potential energy coefficients with $l \geq 1$. Since v_{10} and v_{30} are odd in ρ, they cause transitions from the $|11-\rangle$ state to the $|21+\rangle$ and the $|11+\rangle$ state for example. From Fig. 9, we see that the inelastic cross sections to these two states are indeed approximately equally large. The v_{20} term causes transitions to the $|21-\rangle$ state, and because this expansion coefficient is relatively large, the corresponding cross section is large as well. Finally, in order to change k in the collision, we need potential terms with $m \neq 0$, of which the first two are the v_{33} and the v_{43} coefficients. The v_{33} coefficient causes $-\!\!\rightarrow -$ transitions and the v_{43} coefficient causes $-\!\!\rightarrow +$ transitions. From Fig. 3, we see that the v_{33} coefficient is rather large, explaining the large cross sections to the $|22-\rangle$ state, while the v_{43} coefficient is small, explaining the small cross sections to the $|22+\rangle$ state.

In Fig. 10, we show the integral cross sections for inelastic scattering into the $|32\pm\rangle$ and the $|31\pm\rangle$ states, for a collision energy ranging from the energies at which these channels open, up to 130 cm^{-1}. These small cross sections will be harder to observe experimentally. However, if these channels can be detected, they allow for the observation of pronounced shape resonances at higher collision energies. The cross sections for scattering into the $|32\pm\rangle$ states also give rise to Feshbach resonances with quasi-bound states of $|31\pm\rangle$ character. Even stronger Feshbach resonances at higher collision energies between about 120 and 125 cm^{-1} are found in the cross sections for scattering into the $|31-\rangle$ state. These Feshbach resonances are caused by the opening of the $|44\pm\rangle$ channels at a collision energy of about 125 cm^{-1}.

Finally, we also studied differential cross sections, where we looked in particular at the behavior of the differential cross sections as a function of energy close to resonance. In general, we found that the differential cross sections can change rapidly and dramatically close to resonance. This behavior is illustrated by Fig. 11. Here, we see in the upper two panels, the differential cross sections for elastic scattering at collision energies of 0.87 and 1.86 cm^{-1}. For the first of these energies there is no resonance, while for the second there is a shape resonance. For the off-resonance case we find that, apart from diffraction oscillations, there is only a forward scattering peak. On resonance there is also a strong backward peak. The lower four panels show the differential cross sections for inelastic scattering to the $|11+\rangle$ state at collision energies of 20, 24.36, 30, and 37.28 cm^{-1}. At 20 and 30 cm^{-1}, which are shown in the two lower plots on the left, there is no resonance and the differential cross sections look rather similar to the upper left one, giving predominantly rise to forward scattering. At 24.36 and 37.28 cm^{-1}, which are shown in the two lower plots on the right, there is a Feshbach resonance present, and as a result the differential cross sections look very differently, giving again rise to significant backscattering. In general, the precise structure of the differential cross section depends on various aspects such as the lifetime and the rotational state of the intermediate collision complex. As a result, it is expected that the differential cross sections show clear changes near a resonance, but the precise way in which they change is hard to predict and can be very different for different resonances, as is also seen in Fig. 11.

VI. DISCUSSION AND CONCLUSION

In this article, we have theoretically studied cold collisions of NH_3 molecules with He atoms, where we looked in detail at shape and Feshbach scattering resonances. Prior to collision, we considered the ammonia molecules to be in their antisymmetric umbrella state with angular momentum $j = 1$ and projection $k = 1$, which is a suitable state for Stark deceleration. We calculated state-to-state integral and differential cross sections for collision energies ranging from 10^{-4} cm^{-1} to 130 cm^{-1}, using fully converged quantum close-coupling calculations. We treated the umbrella motion of the ammonia molecule by solving the corresponding Hamiltonian in curvilinear coordinates and taking the resulting first four vibration-tunneling states exactly into account. We call this the elaborate treatment. We also used a common model for the umbrella motion which approximates the umbrella tunneling states as an even and odd combination of the two possible rigid equilibrium structures for ammonia. This we call the model treatment.

To describe the interaction between the NH_3 molecules and the He atoms accurately, we presented a new four-dimensional potential energy surface, based on a high-quality fit of 4180 *ab initio* points. In the short range, we used the explicitly correlated CCSD(T)-F12 method with an AVTZ basis set including midbond functions, and we showed that this approach leads to excellent results in the short range. In the long range, we used the CCSD(T) method with an AVQZ basis but without F12, since we found that the electron density fitting

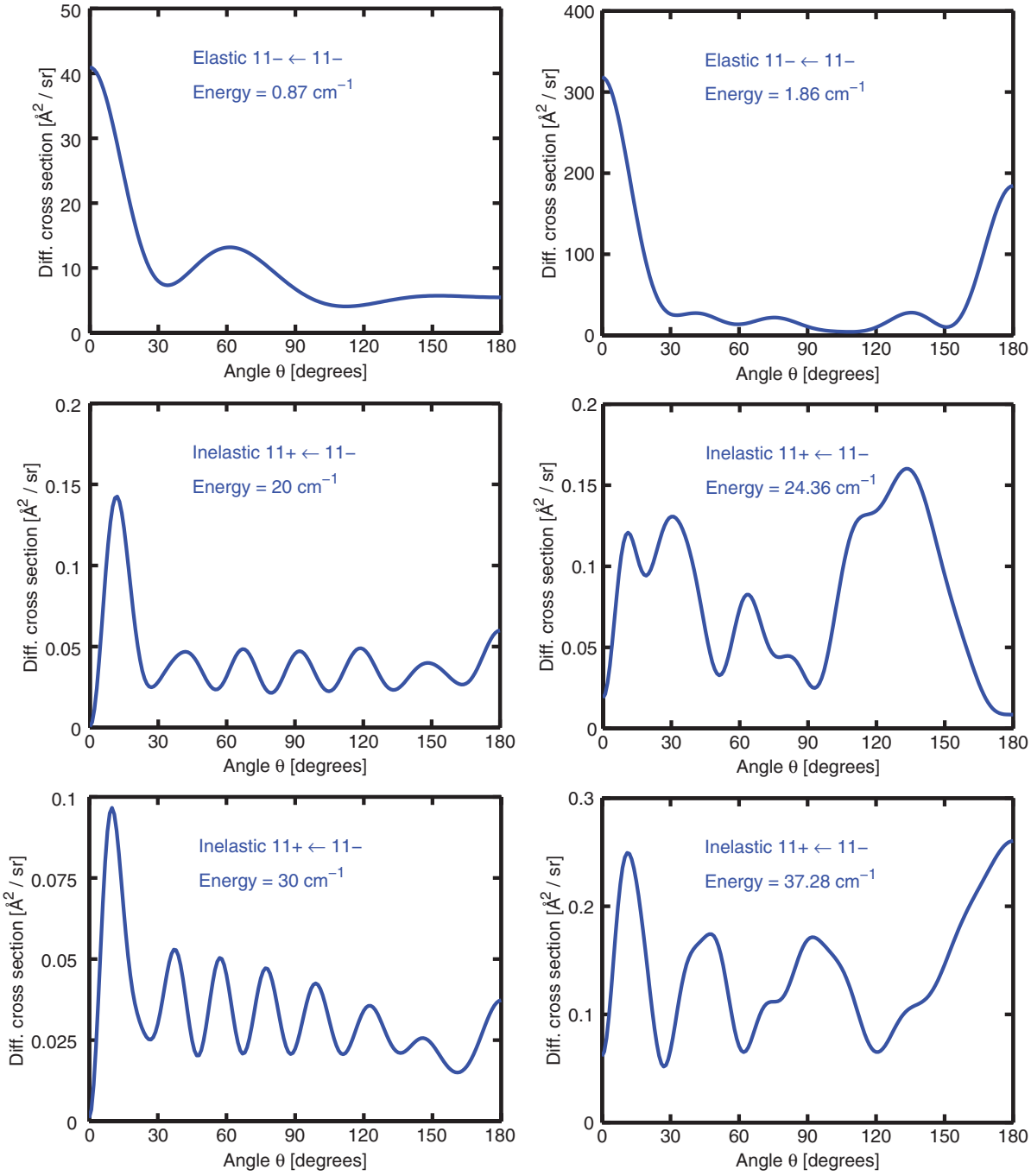

FIG. 11. Differential cross sections as a function of the zenith angle θ for collisions between NH_3 and He at various collision energies. Upper two panels: Differential cross sections for elastic scattering at a collision energy of 0.87 cm^{-1} (left) and 1.86 cm^{-1} (right). In the first case there is no resonance, the second case corresponds to a shape resonance. Middle two panels: Differential cross sections for inelastic scattering into the $|11+\rangle$ state at a collision energy of 20 cm^{-1} (left panel, no resonance) and 24.36 cm^{-1} (right panel, Feshbach resonance). Lower two panels: The same but for a collision energy of 30 cm^{-1} (left panel, no resonance) and 37.28 cm^{-1} (right panel, Feshbach resonance).

that accompanies the F12 treatment does not exactly preserve charge neutrality of the monomers and eventually leads to a dominant $1/R$ dependence of the potential at very large R values. Our potential has a well depth $D_e = 35.08$ cm^{-1}, which is to be compared with the well depth of 33.46 cm^{-1} for the potential of Hodges and Wheatley.[29] Although this difference is not very large, we found that small differences in the potential can have profound consequences for the observed resonance structures at low scattering energies.

We studied all open collision channels for *para* ammonia up to $j = 3$ and in all these channels we found pronounced shape resonances right after the opening of these channels, caused by quasi-bound states in the incoming and outgoing channels. We also found Feshbach resonances that are particularly strong for the outgoing $|11+\rangle$ channel at collision energies of about 25 cm^{-1} caused by intermediate $|22\pm\rangle$ states, and at collision energies of about 35 cm^{-1} caused by intermediate $|21\pm\rangle$ states. Due to the large cross section of these

inelastic resonances, namely more than 1 Å^2, they seem to be a good candidate for experimental observation. Also in the $|31-\rangle$ channel at collision energies of about 120 cm^{-1}, relatively strong Feshbach resonances were seen that are due to intermediate $|44\pm\rangle$ states. We analyzed the observed resonant structures in detail by looking at the corresponding scattering wavefunctions, phase shifts, and lifetimes. We also investigated the validity of using the model treatment for the ammonia umbrella motion in describing low-energy scattering resonances. We found that the model performs qualitatively very well, but on a quantitative level some resonance peaks are somewhat overestimated compared to the elaborate treatment. However, considering the sensitivity of these resonances to the interaction potential, for which even state-of-the-art *ab initio* methods still lead to uncertainties on the order of a percent, the model treatment seems adequate in treating low-energy resonant scattering, especially in cases when the elaborate treatment becomes computationally too expensive.

The calculated integral cross sections at low collision energies can be measured using Stark-decelerated molecular beams. The NH_3 molecule, and its isotopologue ND_3, are amenable to the Stark deceleration technique, and have been employed frequently in deceleration experiments.[56] The Stark decelerator provides a beam of ammonia molecules, state-selected in the upper inversion component of the $j = k = 1$ level, with a velocity that is tunable between standstill and high velocities.[57] In a crossed beam experiment, the Stark decelerated ammonia molecules can be collided with an atomic beam of helium. In an optimized geometry, the two beams collide at a small beam intersection angle. An intersection angle of less than 90° reduces the attainable collision energy and improves the collision energy resolution of the experiment.[58] As shown in Sec. V, there are a number of scattering channels with pronounced shape and/or Feshbach resonances. The most promising prospects for the experimental observation of resonant features are found in the channels $|11+\rangle \leftarrow |11-\rangle$ (see Fig. 5), $|22-\rangle \leftarrow |11-\rangle$, and $|21-\rangle \leftarrow |11-\rangle$ (see Fig. 8).

The resonant structures are found at collision energies in the 20–50 cm^{-1} range. To simulate what would be observed in a molecular beam scattering experiment, we convoluted the integral scattering cross section for the $|11+\rangle \leftarrow |11-\rangle$ inversion inelastic channel with Gaussian collision energy distributions having both a 1 cm^{-1} and a 3 cm^{-1} full width at half maximum (FWHM). In the considered scattering channel bunches of Feshbach resonances are observed that are caused by the opening of the $|22\pm\rangle$ and $|21\pm\rangle$ channels, as seen in Fig. 5. The result of the convolutions are shown in Fig. 12. From this figure, we conclude that the details of the dense resonance structures in Fig. 5 can only be resolved when an experimental collision energy spread that is much less than 1 cm^{-1} can be achieved. For an experimental resolution of 3 cm^{-1}, however, the bunch of scattering resonances can still be discerned from the background inelastic signal by measuring the inelastic cross section as a function of collision energy. Figure 12 shows that such a measurement would lead to a clear enhancement of the inelastic signal by more than a factor of two at the energies where the bunch of resonances is located.

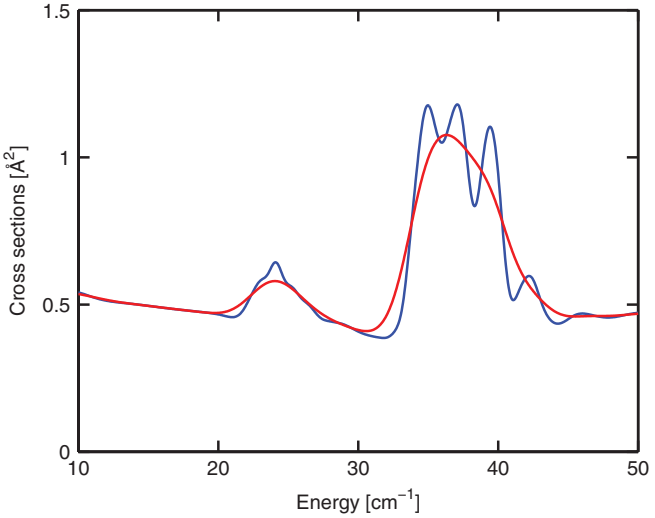

FIG. 12. Convoluted inversion inelastic integral cross sections as a function of the mean collision energy for NH_3-He scattering. The initial state of the NH_3 molecules is the $|11-\rangle$ state and the final state is the $|11+\rangle$ state. The figure is similar to Fig. 5, only now we have assumed a Gaussian collision energy distribution for the colliding particles to simulate more realistically what would be observed with present day experimental technology. The blue curve corresponds to a full width at half maximum of 1 cm^{-1}, and the red curve of 3 cm^{-1}.

To estimate the feasibility of obtaining collision energy resolutions in this range with current experimental technology, we assume an experiment in which a Stark-decelerated packet of NH_3 molecules collides with a conventional beam of He atoms at a beam intersection angle of 45°. We assume that the He atom beam is produced using a cryogenic source that is maintained at a temperature of about 30 Kelvin, resulting in a He atom velocity of 550 m/s. The relevant range of collision energies is then obtained when the velocity of the NH_3 molecules is tuned between 370 and 850 m/s. This is well within the range of state-of-the-art Stark deceleration molecular beam machines.[59] We further assume velocity spreads of 10 m/s and 55 m/s for the NH_3 molecules and He atoms, respectively, and a spread in the beam intersection angle of 40 mrad due to the divergence of both beams. These are values that can realistically be obtained with current experimental techniques. With these parameters, we expect an optimum in the collision energy resolution to occur at a collision energy of 30 cm^{-1}, i.e., at the center of the relevant collision energy range. This maximum accuracy amounts to a spread of 3.1 cm^{-1} (FWHM), while the collision energy spread increases to approximately 4 cm^{-1} both for collision energies down to 20 cm^{-1} and collision energies up to 50 cm^{-1}. These energy resolutions will not yet allow for the observation of single scattering resonances in the NH_3-He system, but they will produce an observable enhancement of about a factor of two in the inelastic cross section as a function of collision energy shown in Fig. 12, revealing the combined effect of the underlying bunch of Feshbach resonances.

An alternative and complementary approach to study scattering resonances is to measure differential cross sections. Referring back to Fig. 11, dramatic changes in the differential cross section can occur at collision energies where a resonance is observed. Feshbach resonances that give rise to

strong backward scattering can be detected by measuring selectively the scattered flux in the backward direction. A similar approach has been used recently to measure partial-wave resolved resonances in the collision energy dependence of reactions between F atoms and HD molecules.[8] For inelastic scattering between NH_3 molecules and He atoms, differential cross sections are measured most conveniently using the velocity map imaging (VMI) technique.[60] To experimentally resolve the angular dependence of the differential cross sections, large recoil velocities of the scattered molecules are advantageous. For the $|11+\rangle \leftarrow |11-\rangle$ channel, the recoil velocity of the scattered NH_3 molecules in the center of mass frame amounts to about 100 m/s at the most relevant collision energies. This is well within the range of velocities that can be imaged using current VMI techniques, offering interesting prospects to study the behavior of molecular scattering resonances.

At the Fritz-Haber-Institute in Berlin, Germany, and the Radboud University Nijmegen, the Netherlands, we have embarked on an experimental program to study scattering resonances in both the integral and differential cross sections using Stark-decelerated molecular beams. It is the hope that the experimental study of these resonances will test our theoretical understanding of molecular interactions with unprecedented accuracy, and also will contribute to an enhancement of our ability to control the way in which molecules collide.

ACKNOWLEDGMENTS

We thank Liesbeth Janssen for helpful discussions. We thank Hans-Joachim Werner for insightful correspondence on the long-range behavior of the CCSD(T)-F12 method. We thank Jeremy Hutson for informing us about the way in which the ammonia inversion model is implemented in MOLSCAT. Koos Gubbels acknowledges support by the European Community's Seventh Framework Program ERC-2009-AdG under grant agreement 247142-MolChip. Sebastiaan Y. T. van de Meerakker acknowledges financial support from Netherlands Organisation for Scientific Research (NWO) via a VIDI grant. Ad van der Avoird thanks the Alexander von Humboldt foundation for a Humboldt Research Award.

APPENDIX: COORDINATES AND SYMMETRY

In this appendix, we consider in more detail the various coordinates used to describe the NH_3-He system and how these coordinates transform under various symmetry operations that commute with the Hamiltonian. These symmetry operations form a group generated by the permutations of the hydrogen atoms in NH_3 and the operator for inversion in space $\hat{E}^*$. The location of the center of mass of the NH_3-He dimer is given by the vector $\mathbf{Q}$, while the locations of the nuclei with respect to $\mathbf{Q}$ are given by the vectors $\mathbf{H}_1$, $\mathbf{H}_2$, and $\mathbf{H}_3$ for the three H atoms, by the vector $\mathbf{N}$ for the N atom, and by **He** for the He atom. The center of mass of the ammonia molecule is given by the vector $\mathbf{X}$. We start by introducing a orthonormal, right-handed space-fixed ("sf") frame centered at the center of mass of the dimer $\mathbf{Q}$. We also make the convention that a superscript denotes the frame in which the coordinates of a vector are expressed. So in the space-fixed frame an arbitrary vector $\mathbf{P}$ has the space-fixed coordinates $\mathbf{P}^{\mathrm{sf}}$. Moreover, when no frame superscript is given, we do not specify the frame in which the coordinates of the vector $\mathbf{P}$ are evaluated. The space-fixed frame consists of three unit vectors, which are the columns of the matrix $\mathbf{s} = (\mathbf{s}_x, \mathbf{s}_y, \mathbf{s}_z)$. In our notation, $\mathbf{s}^{\mathrm{sf}}$ is the unit matrix. Moreover, in the space-fixed frame the inversion operator $\hat{E}^*$ maps the position of any nucleus $\mathbf{P}^{\mathrm{sf}}$ onto the position reflected in the origin $-\mathbf{P}^{\mathrm{sf}}$.

Another useful frame, the dimer frame or body-fixed frame $\mathbf{d} = (\mathbf{d}_x, \mathbf{d}_y, \mathbf{d}_z)$, is obtained by performing two rotations to the space-fixed frame in order to align the $\mathbf{d}_z$ axis of the dimer frame along the vector $\mathbf{R} = \mathbf{He} - \mathbf{X}$, which points from the center of mass of the ammonia molecule to the helium atom. We have in space-fixed coordinates that

$$\mathbf{R}^{\mathrm{sf}} = \begin{pmatrix} R\cos\phi^{\mathrm{sf}}\sin\theta^{\mathrm{sf}} \\ R\sin\phi^{\mathrm{sf}}\sin\theta^{\mathrm{sf}} \\ R\cos\theta^{\mathrm{sf}} \end{pmatrix}, \tag{A1}$$

so that ϕ^{sf} and θ^{sf} are the azimuth and zenith angle of the vector $\mathbf{R}$ in the space-fixed frame. The body-fixed frame is then defined in the following way. For any vector $\mathbf{P}$, we have that $\mathbf{P} = \mathbf{s} \cdot \mathbf{P}^{\mathrm{sf}} = \mathbf{d} \cdot \mathbf{P}^{\mathrm{bf}}$ with $\mathbf{P}^{\mathrm{sf}} = \mathcal{R}^{\mathrm{sf}}_{\mathrm{bf}} \cdot \mathbf{P}^{\mathrm{bf}}$ and $\mathcal{R}^{\mathrm{sf}}_{\mathrm{bf}} = \mathcal{R}_z(\phi^{\mathrm{sf}})\mathcal{R}_y(\theta^{\mathrm{sf}})$, where $\mathcal{R}_y(\theta^{\mathrm{sf}})$ and $\mathcal{R}_z(\phi^{\mathrm{sf}})$ are the usual rotation matrices for rotation about the y axis and the z axis, respectively, with the convention that $\mathcal{R}_z(\phi^{\mathrm{sf}})_{12} = -\sin\phi^{\mathrm{sf}}$ and $\mathcal{R}_y(\theta^{\mathrm{sf}})_{31} = -\sin\theta^{\mathrm{sf}}$. Note that as a result, we find for the coordinates of the vector $\mathbf{R}$ in the body-fixed frame that $(\mathcal{R}^{\mathrm{sf}}_{\mathrm{bf}})^T\mathbf{R}^{\mathrm{sf}} = \mathbf{R}^{\mathrm{bf}}$ resulting in $R^{\mathrm{bf}}_x = R^{\mathrm{bf}}_y = 0$ and $R^{\mathrm{bf}}_z = R$, as was required. When we apply the $\hat{E}^*$ operator to the complex, the coordinates $\mathbf{R}^{\mathrm{sf}}$ get inverted, so that $\hat{E}^*$: $\mathbf{R}^{\mathrm{sf}} \rightarrow -\mathbf{R}^{\mathrm{sf}}$. As a result, the angles in Eq. (A1) are changed according to $\phi^{\mathrm{sf}} \rightarrow \phi^{\mathrm{sf}} + \pi$ and $\theta^{\mathrm{sf}} \rightarrow \pi - \theta^{\mathrm{sf}}$. Note that the dimer frame is invariant under permutations of the hydrogen atoms.

The third useful frame is called the monomer frame and it is located at the center of mass of the ammonia molecule $\mathbf{X}$. The frame is spanned by the vectors,

$$\begin{aligned} \mathbf{v}_x &= 2\mathbf{H}_1 - \mathbf{H}_2 - \mathbf{H}_3, \\ \mathbf{v}_y &= \mathbf{H}_2 - \mathbf{H}_3, \\ \mathbf{v}_z &= \mathbf{v}_x \times \mathbf{v}_y. \end{aligned} \tag{A2}$$

Since the ammonia molecule keeps its threefold symmetry, the above frame is orthogonal. The monomer frame can consequently be made orthonormal by dividing the vectors in Eq. (A2) by their length, resulting in the right-handed monomer frame denoted by $\mathbf{f}$. The rotation matrix that expresses the monomer frame axes in space-fixed coordinates is given in terms of the three Euler angles $\zeta^{\mathrm{sf}} = (\alpha^{\mathrm{sf}}, \beta^{\mathrm{sf}}, \gamma^{\mathrm{sf}})$, resulting in $\mathcal{R}^{\mathrm{sf}}_{\mathrm{mf}} = \mathcal{R}_z(\alpha^{\mathrm{sf}})\mathcal{R}_y(\beta^{\mathrm{sf}})\mathcal{R}_z(\gamma^{\mathrm{sf}})$. When the $\hat{E}^*$ operator is applied to the complex, then both the x axis and the y axis of the monomer frame are reversed in the space-fixed frame, which leaves the z axis in place. As a result, the $\hat{E}^*$ operator has the following effect on the Euler angles, $\hat{E}^*$: $\alpha^{\mathrm{sf}} \rightarrow \alpha^{\mathrm{sf}}$, $\beta^{\mathrm{sf}} \rightarrow \beta^{\mathrm{sf}}$, and $\gamma^{\mathrm{sf}} \rightarrow \gamma^{\mathrm{sf}} + \pi$. Another angle that is important in our treatment of the ammonia-helium complex is the inversion or umbrella angle ρ, defined as the angle between the z axis of the monomer frame and the vector pointing

TABLE II. Transformation properties of the coordinates under symmetry operations.

Operation	Effect on angular coordinates								
$\hat{E}$	$\theta^{\rm sf}$	$\phi^{\rm sf}$	ρ	$\alpha^{\rm sf}$	$\beta^{\rm sf}$	$\gamma^{\rm sf}$	$\alpha^{\rm bf}$	$\beta^{\rm bf}$	$\gamma^{\rm bf}$
(123)	$\theta^{\rm sf}$	$\phi^{\rm sf}$	ρ	$\alpha^{\rm sf}$	$\beta^{\rm sf}$	$\gamma^{\rm sf}-2\pi/3$	$\alpha^{\rm bf}$	$\beta^{\rm bf}$	$\gamma^{\rm bf}-2\pi/3$
(23)*	$\pi-\theta^{\rm sf}$	$\phi^{\rm sf}+\pi$	ρ	$\alpha^{\rm sf}+\pi$	$\pi-\beta^{\rm sf}$	$\pi-\gamma^{\rm sf}$	$\pi-\alpha^{\rm bf}$	$\beta^{\rm bf}$	$-\gamma^{\rm bf}$
$\hat{E}^*$	$\pi-\theta^{\rm sf}$	$\phi^{\rm sf}+\pi$	$\pi-\rho$	$\alpha^{\rm sf}$	$\beta^{\rm sf}$	$\gamma^{\rm sf}+\pi$	$-\alpha^{\rm bf}$	$\pi-\beta^{\rm bf}$	$\gamma^{\rm bf}$
(123)*	$\pi-\theta^{\rm sf}$	$\phi^{\rm sf}+\pi$	$\pi-\rho$	$\alpha^{\rm sf}$	$\beta^{\rm sf}$	$\gamma^{\rm sf}+\pi/3$	$-\alpha^{\rm bf}$	$\pi-\beta^{\rm bf}$	$\gamma^{\rm bf}-2\pi/3$
(23)	$\theta^{\rm sf}$	$\phi^{\rm sf}$	$\pi-\rho$	$\alpha^{\rm sf}+\pi$	$\pi-\beta^{\rm sf}$	$-\gamma^{\rm sf}$	$\alpha^{\rm bf}+\pi$	$\pi-\beta^{\rm bf}$	$-\gamma^{\rm bf}$

from the N atom to one of the H atoms. So, for $\rho=\pi/2$, ammonia has a planar geometry. We just showed that $\hat{E}^*$ leaves the z axis in place, while the coordinates of the nuclei change sign. As a result, we have that $\hat{E}^*$: $\rho\rightarrow\pi-\rho$.

When we permute the hydrogen nuclei, the space-fixed coordinates of the monomer frame axes are changed. For example, when we interchange $\vec{\mathbf{H}}_2$ and $\vec{\mathbf{H}}_3$ we find that the monomer y axis and also the z axis are reversed in the space-fixed frame. As a result, the corresponding Euler angles transform as (23): $\alpha^{\rm sf}\rightarrow\pi+\alpha^{\rm sf}$, $\beta^{\rm sf}\rightarrow\pi-\beta^{\rm sf}$, and $\gamma^{\rm sf}\rightarrow-\gamma^{\rm sf}$. Since the (23) operation inverts the monomer z axis, we also find that (23): $\rho\rightarrow\pi-\rho$. In Table II, we show the transformation properties of the various angles that describe the ammonia-helium complex when symmetry operations of the permutation-inversion group D_{3h}(M) are applied to the complex. These transformation properties are useful in determining the transformation properties of the angular basis functions.

The monomer frame can also be obtained by a rotation from the body-fixed dimer frame rather than the space-fixed frame, defining the body-fixed Euler angles $\zeta^{\rm bf}=(\alpha^{\rm bf},\beta^{\rm bf},\gamma^{\rm bf})$. The rotation matrix that expresses the monomer frame axes in body-fixed coordinates is given by $\boldsymbol{\mathcal{R}}^{\rm bf}_{\rm mf}=\boldsymbol{\mathcal{R}}_z(\alpha^{\rm bf})\boldsymbol{\mathcal{R}}_y(\beta^{\rm bf})\boldsymbol{\mathcal{R}}_z(\gamma^{\rm bf})$. When the hydrogen atoms are permuted, the body-fixed frame is unchanged, and as a result the body-fixed Euler angles transform in precisely the same way as the space-fixed ones. However, when $\hat{E}^*$ is applied, not only the monomer frame axes in space-fixed coordinates change, but also the dimer frame axes. As a result, the body-fixed Euler angles transform somewhat differently than the space-fixed angles, as seen in Table II.

Having determined the effect of the various symmetry operations on the coordinates that describe the NH_3-He complex, we can also find out the corresponding effect on the angular basis functions of Eqs. (5) and (7) by using the transformation properties of the Wigner d-functions. Moreover, we have that $\hat{E}^*\phi_v^{\pm}(\rho)=\pm\phi_v^{\pm}(\rho)$. The effect of the various symmetry operations on the angular basis functions is shown in Table III.

As a result, we are now able to construct the symmetry adapted basis sets for both the body-fixed and the space-fixed case. To this end, it is most convenient to start by discussing the symmetry group C_{3v}(M) with irreps A_1, A_2, and E. The C_{3v}(M) group is generated by the operations $\hat{E}$, (123), and (23)*. Using this group implies that we consider the ammonia molecule as a rigid rotor without umbrella motion. Then, for the body-fixed case with $k=K=0$, we conclude from Table III that the state $|j00JM\rangle$ is of A_1 symmetry when J is even, while it is of A_2 symmetry when J is odd. When either k or K is nonzero, we have for $k=0$ (mod 3) that $(|jKJM\rangle+(-1)^{J+k}|j\ -k\ -KJM\rangle)/2^{1/2}$ is of A_1 symmetry, while $(|jkKJM\rangle-(-1)^{J+k}|j\ -k\ -KJM\rangle)/2^{1/2}$ is of A_2 symmetry. Finally, we have for $k\neq0$ (mod 3), that two-dimensional E irreps are spanned by the states $(|jKJM\rangle, |j\ -k\ -KJM\rangle)$.

For the space-fixed case and considering rigid ammonia, we conclude from Table III that the state $|j0LJM\rangle$ is of A_1 symmetry when $j+L$ is even, while it is of A_2 symmetry when $j+L$ is odd. When k is nonzero and a multiple of 3, we have that $(|jkLJM\rangle+(-1)^{j+L+k}|j\ -kLJM\rangle)/2^{1/2}$ is of A_1 symmetry, while $(|jkLJM\rangle-(-1)^{j+L+k}|j\ -kLJM\rangle)/2^{1/2}$ is of A_2 symmetry. For $k\neq0$ (mod 3), we have that two-dimensional E irreps are spanned by the states $\{|jkLJM\rangle, |j\ -kLJM\rangle\}$.

Finally, the complete symmetry adapted basis is obtained by considering the full D_{3h}(M) symmetry group of the non-rigid ammonia molecule. The functions adapted to the irreps of D_{3h}(M) are obtained from those adapted to the C_{3v}(M) irreps by using

$$\begin{aligned}
&(\hat{E}+\hat{E}^*)|A_1\rangle=|A_1'\rangle, \quad (\hat{E}-\hat{E}^*)|A_1\rangle=|A_2''\rangle,\\
&(\hat{E}+\hat{E}^*)|A_2\rangle=|A_2'\rangle, \quad (\hat{E}-\hat{E}^*)|A_2\rangle=|A_1''\rangle,\\
&(\hat{E}+\hat{E}^*)|E\rangle=|E'\rangle, \quad (\hat{E}-\hat{E}^*)|E\rangle=|E''\rangle.
\end{aligned} \tag{A3}$$

TABLE III. Effect of the symmetry operations on the angular basis functions.

Operation	Body-fixed	Space-fixed
$\hat{E}$	$\lvert jkKJMv^{\pm}\rangle$	$\lvert jkLJMv^{\pm}\rangle$
(123)	$e^{2\pi ik/3}\lvert jkKJMv^{\pm}\rangle$	$e^{2\pi ik/3}\lvert jkLJMv^{\pm}\rangle$
(23)*	$\pm(-1)^{J+k}\lvert j\ -k\ -KJMv^{\pm}\rangle$	$\pm(-1)^{j+k+L}\lvert j\ -kLJMv^{\pm}\rangle$
$\hat{E}^*$	$\pm(-1)^{J+j+k}\lvert jk\ -KJMv^{\pm}\rangle$	$\pm(-1)^{L+k}\lvert jkLJMv^{\pm}\rangle$
(123)*	$\pm(-1)^{J+j+k}e^{2\pi ik/3}\lvert jk\ -KJMv^{\pm}\rangle$	$\pm e^{2\pi ik/3}\lvert jkLJMv^{\pm}\rangle$
(23)	$(-1)^j\lvert j\ -kKJMv^{\pm}\rangle$	$(-1)^j\lvert j\ -kLJMv^{\pm}\rangle$

Further we note that the v^+ umbrella functions belong to the $(\hat{E} + \hat{E}^*)$ projection, while the v^- umbrella functions belong to the $(\hat{E} - \hat{E}^*)$ projection.

[1] *Ultra-Cold Fermi Gases*, edited by M. Inguscio, W. Ketterle, and C. Salomon (IOS, Amsterdam, 2008); Proceedings of the International School of Physics Enrico Fermi, Course CLXIV, Varenna, 20–30 June 2006.
[2] H. T. C. Stoof, K. B. Gubbels, and D. B. M. Dickerscheid, *Ultracold Quantum Fields* (Springer, Dordrecht, 2009).
[3] A. Schutte, D. Bassi, F. Tommasini, and G. Scoles, Phys. Rev. Lett. **29**, 979 (1975).
[4] J. P. Toennies, W. Welz, and G. Wolf, J. Chem. Phys. **71**, 614 (1979).
[5] R. T. Skodje, D. Skouteris, D. E. Manolopoulos, S.-H. Lee, F. Dong, and K. Liu, Phys. Rev. Lett. **85**, 1206 (2000).
[6] R. T. Skodje, D. Skouteris, D. E. Manolopoulos, S.-H. Lee, F. Dong, and K. Liu, J. Chem. Phys. **112**, 4536 (2000).
[7] M. H. Qiu, Z. F. Ren, L. Che, D. X. Dai, S. A. Harich, X. Y. Wang, X. M. Yang, C. X. Xu, D. Q. Xie, M. Gustafsson, R. T. Skodje, Z. G. Sun, and D. H. Zhang, Science **311**, 1440 (2006).
[8] W. Dong, C. Xiao, T. Wang, D. X. Dai, X. M. Yang, and D. H. Zhang, Science **327**, 1501 (2010).
[9] J. J. Gilijamse, S. Hoekstra, S. Y. T. van de Meerakker, G. C. Groenenboom, and G. Meijer, Science **313**, 1617 (2006).
[10] H. L. Bethlem, G. Berden, and G. Meijer, Phys. Rev. Lett. **83**, 1558 (1999).
[11] L. Scharfenberg, J. Kłos, P. J. Dagdigian, M. H. Alexander, G. Meijer, and S. Y. T. van de Meerakker, Phys. Chem. Chem. Phys. **12**, 10660 (2010).
[12] M. Kirste, L. Scharfenberg, J. Kłos, F. Lique, M. H. Alexander, G. Meijer, and S. Y. T. van de Meerakker, Phys. Rev. A **82**, 042717 (2010).
[13] L. Scharfenberg, K. B. Gubbels, M. Kirste, G. C. Groenenboom, A. van der Avoird, G. Meijer, and S. Y. T. van de Meerakker, Eur. Phys. J. D **65**, 189 (2011).
[14] A. van der Avoird, P. E. S. Wormer, and R. Moszynski, Chem. Rev. **94**, 1931 (1994).
[15] P. E. S. Wormer and A. van der Avoird, Chem. Rev. **100**, 4109 (2000).
[16] M. Slipchenko and A. Vilesov, Chem. Phys. Lett. **412**, 176 (2005).
[17] A. C. Cheung, D. M. Rank, C. H. Townes, D. D. Thornton, and W. J. Welch, Phys. Rev. Lett. **21**, 1701 (1968).
[18] T. Oka, J. Chem. Phys. **49**, 3135 (1968).
[19] H. Meyer, U. Buck, R. Schinke, and G. Diercksen, J. Chem. Phys. **86**, 4976 (1986).
[20] T. Seelemann, P. Andresen, J. Schleipen, B. Beyer, and J. J. ter Meulen, Chem. Phys. **126**, 27 (1988).
[21] J. Schleipen and J. J. ter Meulen, Chem. Phys. **156**, 479 (1991).
[22] H. Meyer, J. Chem. Phys. **99**, 1101 (1995).
[23] S. Green, J. Chem. Phys. **64**, 3463 (1976).
[24] G. D. Billing, L. L. Poulsen, and G. H. F. Diercksen, Chem. Phys. **98**, 397 (1985).
[25] J. Chen and Y. Zhang, J. Phys. B **30**, 347 (1997).
[26] W. F. Wang, Chem. Phys. **288**, 23 (2003).
[27] U. Machin and E. Roueff, J. Phys. B **30**, 1519 (2005).
[28] B. Yang and P. Stancil, Eur. Phys. J. D **47**, 351 (2008).
[29] M. P. Hodges and R. J. Wheatley, J. Chem. Phys. **114**, 8836 (2001).
[30] J. W. I. van Bladel, A. van der Avoird, and P. E. S. Wormer, J. Phys. Chem. **95**, 5414 (1991).
[31] J. W. I. van Bladel, A. van der Avoird, and P. E. S. Wormer, Chem. Phys. **165**, 47 (1992).
[32] X. Huang, D. W. Schwenke, and T. J. Lee, J. Chem. Phys. **129**, 214304 (2008).
[33] C. H. Townes and A. L. Schawlow, *Microwave Spectroscopy* (Dover, New York, 1975).
[34] P. R. Bunker and P. Jensen, *Molecular Symmetry and Spectroscopy*, 2nd ed. (NRC Research Press, Ottawa, 1998).
[35] B. R. Johnson, J. Comput. Phys. **13**, 445 (1973).
[36] M. S. Child, *Molecular Collision Theory* (Academic, London, 1974).
[37] H.-J. Werner, P. J. Knowles, R. Lindh, F. R. Manby, M. Schütz *et al.*, MOLPRO, version 2009.1, a package of *ab initio* programs, 2009, see http://www.molpro.net.
[38] S. F. Boys and F. Bernardi, Mol. Phys. **19**, 553 (1970).
[39] K. Raghavachari, G. W. Trucks, J. A. Pople, and M. Head-Gordon, Chem. Phys. Lett. **157**, 479 (1989).
[40] T. H. Dunning, Jr., J. Chem. Phys. **90**, 1007 (1989).
[41] D. Woon and T. H. Dunning, Jr., J. Chem. Phys. **100**, 2975 (1994).
[42] T. B. Adler, G. Knizia, and H.-J. Werner, J. Chem. Phys. **127**, 221106 (2007).
[43] H. Koch, B. Fernández, and O. Christiansen, J. Chem. Phys. **108**, 2784 (1998).
[44] A. van der Avoird, P. E. S. Wormer, F. Mulder, and R. M. Berns, Top. Curr. Chem. **93**, 1 (1980).
[45] K. T. Tang and J. P. Toennies, J. Chem. Phys. **80**, 3726 (1984).
[46] T.-S. Ho and H. Rabitz, J. Chem. Phys. **104**, 2584 (1996).
[47] See supplementary material at http://dx.doi.org/10.1063/1.3683219 for the fit of the potential energy surface and for the *ab initio* data points.
[48] G. C. Groenenboom and D. T. Colbert, J. Chem. Phys. **99**, 9681 (1993).
[49] S. L. Davis and J. E. Boggs, J. Chem. Phys. **69**, 2355 (1978).
[50] S. Green, J. Chem. Phys. **73**, 2740 (1980).
[51] J. M. Hutson and S. Green, molscat computer code, version 14 (1994), distributed by Collaborative Computational Project No. 6 of the Engineering and Physical Sciences Research Council (UK).
[52] G. C. M. van der Sanden, P. E. S. Wormer, A. van der Avoird, J. Schleipen, and J. J. ter Meulen, J. Chem. Phys. **97**, 6460 (1992).
[53] E. P. Wigner, Phys. Rev. **73**, 1002 (1948).
[54] C. J. Ashton, M. S. Child, and J. M. Hutson, J. Chem. Phys. **78**, 4025 (1983).
[55] J. Millan, N. Halberstadt, G. C. M. van der Sanden, and A. van der Avoird, J. Chem. Phys. **103**, 4138 (1995).
[56] H. L. Bethlem, F. M. H. Crompvoets, R. T. Jongma, S. Y. T. van de Meerakker, and G. Meijer, Phys. Rev. A **65**, 053416 (2002).
[57] C. E. Heiner, H. L. Bethlem, and G. Meijer, Phys. Chem. Chem. Phys. **8**, 2666 (2006).
[58] L. Scharfenberg, S. Y. T. van de Meerakker, and G. Meijer, Phys. Chem. Chem. Phys. **13**, 8448 (2011).
[59] L. Scharfenberg, H. Haak, G. Meijer, and S. Y. T. van de Meerakker, Phys. Rev. A **79**, 023410 (2009).
[60] A. T. J. B. Eppink and D. H. Parker, Rev. Sci. Instrum. **68**, 3477 (1997).